Volume 1 | Number 1 | Jan 2013 | Pages 1–100

## Dalton Transactions

An international journal of inorganic chemistry
www.rsc.org/dalton

ROYAL SOCIETY OF CHEMISTRY

ROYAL SOCIETY OF CHEMISTRY

www.rsc.org/dalton

# Journal Name

## ARTICLE

# Synthesis of mesoporous Beta and Sn-Beta zeolites and their catalytic performances

Junjiang Jin,[a] Xinxin Ye,[b] Yongsheng Li,[a] Yanqin Wang,[b] Liang Li,[a] Jinlou Gu,[a] Wenru Zhao[a] and Jianlin Shi[c] ,

Mesoporous Beta zeolite has been successfully prepared through hydrothermal synthesis in the presence of cationic ammonium-modified chitosan as the meso-template. Through a subsequent solid-gas reaction between highly dealuminated mesoporous Beta zeolite and $SnCl_4$ steam at an elevated temperature, mesoporous Sn-Beta has been facilely obtained. It was revealed that the addition of cationic chitosan induced the nanocrystal aggregation to particle sizes of ~ 300 nm, giving rise to the intercrystalline/interparticle mesoporosity. In the Sn-implanting procedure, Sn species were demonstrated to be doped into the framework of the resulting mesoporous Beta zeolite in a tetrahedral environment without structural collapse. Due to the micro/mesoporous structures, both mesoporous Beta and Sn-Beta exhibited superior performances in α-pinene isomerization, Baeyer-Villiger oxidation of 2-adamantanone by hydrogen peroxide and the isomerization of glucose in water, respectively.

## Introduction

Aluminosilicate zeolites and zeolitic metallosilicate containing isolated transition metal ions have been extensively used as solid Bronsted acid catalysts in petrochemical processing and solid Lewis acid catalysts for redox reactions, due to their uniform, small pore size, flexible frameworks, and controlled chemistry. [1] However, their applications are limited to small molecules that can diffuse through the narrow channels (< 0.8 nm) and small cavities (< 1.5 nm typically). [1a, b, 2] It has been widely demonstrated that the mass transfer limitations are an important issue in industrial application involving zeolitic materilas. [3] To circumvent the diffusional limitations imposed by zeolitic structures, several strategies have been pursued, such as the synthesis of zeolite nanocrystals, [3d, 4] ultra-large pore zeolites, [1a, b, 5] supported zeolite nanocrystals [6] and inserting larger pores into the zeolite particles [3b, c, 7].

Zeolite nanocrystals can expose more active sites than conventional zeolite crystals due to their higher external to internal surface ratio. However, the synthesized zeolites with particle size smaller than 100 nm would cause a decrease in micropore volume. [3b, 8] Moreover, nanozeolite powders are generally produced at low yields and their isolation is time-consuming and costly. [2a, 7e] The success in synthesizing ultra-large pore zeolites provides an alternative choice. However, the increases in pore size were modest even specific organic structure directing agents were employed. [9] Furthermore, the lack of chemical and thermal stability as well as the high cost often hinders their wide application in industry. With respect to supported zeolite crystals, hydrothermally stable and alkali-tolerable porous supports are highly required, which can preserve their initial porous structures. [10] Hierarchical zeolites, where mesoporosity and/or macroporosity are introduced into the microporous framework of zeolites, are regarded as the

most promising materials. Nevertheless, the term mostly refers to mesoporous zeolites, i.e. hierarchical zeolites featuring additional porosity in the mesopore size region (pore diameters in the range 2-50 nm) because the major impact of auxiliary porosity on catalysis stems from porosity in this size region. [7d, 11]

In the last decade, various strategies have been developed to synthesize zeolites with additional mesoporosity. Briefly, these strategies can be classified into four categories: (a) direct synthesis using different dual templating strategies, including the common zeolite structure directing agents and additional secondary templates for mesostructuring the zeolite crystals [12]; (b) direct synthesis using only single but multi-functional template, containing structure directing fragments for the micro- and mesoscale in the same molecule [13]; (c) generation of mesopores in zeolite single crystals by post-synthesis treatment [14]; (d) synthetic route relying on specific reaction conditions that make secondary templates unnecessary [15]. Particularly, some strategies have shown good versatility in the synthesis of different-structured zeolites. [7, 16] However, few attention has been devoted to fabricating mesoporous zeolitic metallosilicate with high crystallinity by a simple templating route probably due to their special synthetic conditions involved, such as the introduction of the fluoride anion as the mineralizing agent. [17] Alternatively, to insert heteroatoms into the framework of zeolites, several post-synthetic strategies have been developed, such as solid-gas implanting, solid-state ion-exchange and impregnation. [18] Thus, the combination of hydrothermal synthesis of mesoporous zeolites using secondary templates and a subsequent post-synthetic route may open a door to obtain mesoporous zeolitic metallosilicate. Sn-Beta, a Tin-containing molecular sieve with the zeolite Beta topology, has received great attentions in biocatalysis because of its superiority in activating carbonyl groups. [17c, d, 19] However, to

the best of our knowledge, very few researches about mesoporous Sn-Beta have been published. [18c]

In this work, mesoporous Beta zeolite was firstly synthesized through a hydrothermal method in the presence of a cationic derivate of chitosan, though chitosan has been widely used in preparation of organic/inorganic composites [20]. Following a dealumination process, post-synthesis was carried out to obtain mesoporous Sn-Beta through the solid-gas reaction of highly dealuminated Beta zeolite and $SnCl_4$ vapor at an elevated temperature. The physicochemical properties of the obtained products were characterized by several techniques, including XRD, $N_2$ adsorption, SEM, TEM, NMR spectroscopy, TGA, UV-Vis spectroscopy and temperature-programmed desorption ($NH_3$-TPD). Their catalytic behaviours were evaluated in α-pinene isomerization, selective oxidation of 2-adamantanone by hydrogen peroxide and the isomerization of glucose in water, respectively.

## Results and discussion

### 1. Mesoporous Beta zeolite

Fig. 1 shows the XRD patterns of the synthesized mesoporous Beta zeolite (Meso-Beta) and conventional beta (Con-Beta). As can be seen, both Meso-Beta and Con-Beta exhibit a series of diffraction peaks located at 7.8 °, 13.4 °, 14.5°, 21.5° and 22.5°, respectively, characteristic of BEA structure [21]. This indicates that the addition of cationic chitosan has not affected the crystallization of Beta zeolite. By taking the Con-Beta zeolite as a reference, the crystallinity of Meso-Beta is estimated to be about 89%.
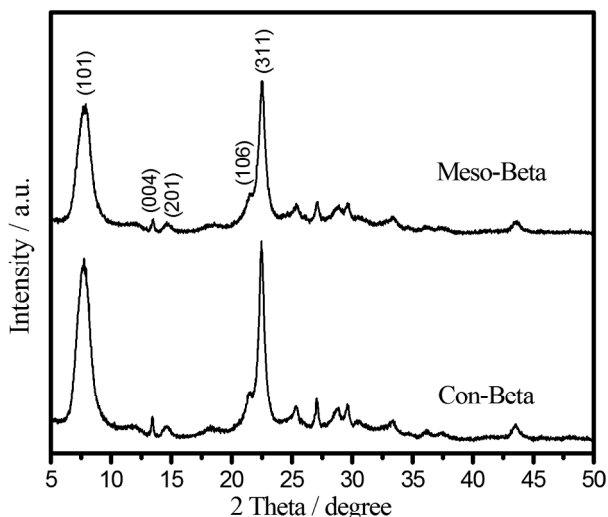


Figure 1. XRD patterns of Meso-Beta and Con-Beta.

The $N_2$ adsorption-desorption isotherms and the corresponding BJH pore size distributions of Meso-Beta and Con-Beta are shown in Fig. 2 and the corresponding structural properties are presented in Table 1. In addition to the representative type I isotherm characteristic of microporous materials, Meso-Beta presents a steep leap and a hysteresis loop at $P/P_0$ region of 0.88 ~ 0.97, indicating the presence of mesoporosity with large pore sizes. From the corresponding pore size distribution derived from the desorption branch of the isotherm using the Barrett-Joyner-Halenda (BJH) method, the mesopore size is estimated to be 20 ~ 50 nm. As listed in Table 1, significant increases in the total and external specific surface area, total and external pore volume are clearly observed. These can be attributed to the generation of mesoporosity in the

sample of Meso-Beta. Meanwhile, it is worth noting that the decrease in the micropore volume and micropore surface area is almost negligible.
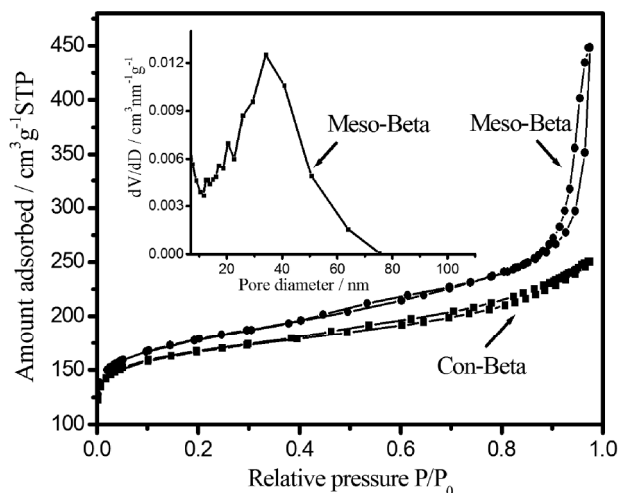


Figure 2. $N_2$ adsorption-desorption isotherms and pore-size distribution curve (inset) of Con-Beta and Meso-Beta.

Table 1. Textural properties of the samples [a]

| Sample | Si/Al | Sn (wt%) | $S_{BET}$ ($m^2g^{-1}$) | $S_{micro}$ ($m^2g^{-1}$) | $S_{external}$ ($m^2g^{-1}$) | $V_{total}$ ($cm^3g^{-1}$) | $V_{micro}$ ($cm^3g^{-1}$) | $V_{external}$ ($cm^3g^{-1}$) | Pore diameter (nm) |
|---|---|---|---|---|---|---|---|---|---|
| Meso-Beta | 9.0 | - | 660 | 477 | 183 | 0.69 | 0.20 | 0.49 | 20-50 |
| Con-Beta | 8.7 | - | 629 | 503 | 126 | 0.39 | 0.21 | 0.18 | - |
| H-Al-Meso-Beta | 9.1 | - | 643 | 429 | 214 | 0.61 | 0.18 | 0.43 | 20-50 |
| De-Al-Meso-Beta | >1500 | - | 595 | 380 | 215 | 0.63 | 0.15 | 0.48 | 20-50 |
| Meso-Sn-Beta | >1500 | 1.1 | 623 | 405 | 218 | 0.51 | 0.17 | 0.34 | 20-50 |
| Con-Sn-Beta | >2000 | 1.2 | 589 | 544 | 45 | 0.27 | 0.21 | 0.06 | - |

[a] Si/Al ratio and Sn content were measured by inductively coupled plasma (ICP) analysis; BET surface area ($S_{BET}$) is calculated from Brunauer-Emmett-Teller method; the micropore surface area ($S_{micro}$), external specific surface area ($S_{external}$) and the micropore volume ($V_{micro}$) are calculated from t-plot method; the total pore volume ($V_{total}$) is evaluated at $P/P_0$=0.98; the external pore volume ($V_{external}$) is calculated according to $V_{total} - V_{micro}$; the diameter of mesopore is estimated from BJH method using the desorption branch of the isotherm curves.

Transmission electron microscopy (TEM) images, as shown in Fig. 3a and b, confirm the co-existence of micropores and mesopores in Meso-Beta sample. Notably, Meso-Beta particles contain plenty of stacked zeolite nanocrystals, which are believed to contribute to the mesoporosity. In the enlarged TEM image (Fig. 3b and inset), randomly oriented microporous channels in the Meso-Beta partilce can be observed, indicating that mesoporosity was formed by the aggregation of nanocrystals. Scanning electron microscopy (SEM) images provide more detailed insights into the morphology and structure of the samples. As presented in Fig. 3c and d, Meso-Beta particles possess irregular morphology of about 300 nm in diameters and are composed of closely stacked zeolite nanocrystals (30 ~ 40 nm in size). In addition to the intercrystal mesoporosity, the interparticle voids are proposed to contribute to the mesoporosity to some extent. In contrast, Con-Beta contains bulky particles (about 2 μm in diameters) with rough surface but without visible porous structure. These results demonstrate that the addition of cationic chitosan not only acts as a meso-template by aggregating nanocrystals, but also decreases the dimension of zeolite particles by hindering their further growth. [22]
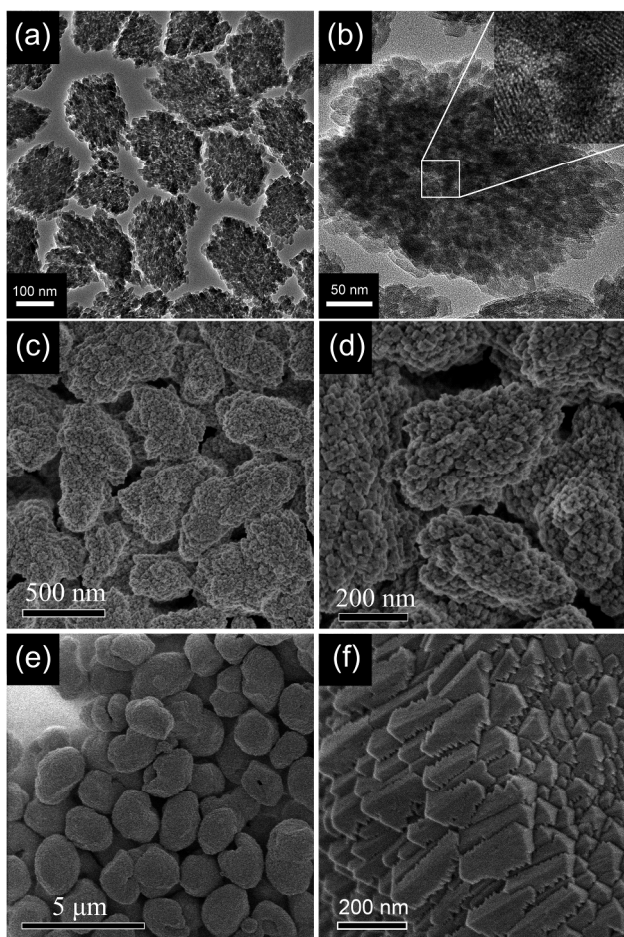
Figure 3. TEM images (a, b) of Meso-Beta; SEM images of Meso-Beta (c, d) and Con-Beta (e, f) at different magnifications.

The structural configuration and local environment of Si and Al atoms in Meso-Beta and Con-Beta were investigated by $^{29}$Si and $^{27}$Al MAS NMR spectroscopy, as given in Fig. S1. It is found that Meso-Beta displays similar $^{29}$Si NMR spectrum with Con-Beta. Two major peaks at $\delta$ = -116 ppm and -108 ppm corresponding to Si(4Si) species and the peak at -104 ppm resulting from both Si(3Si, 1Al) or Si(3Si, 1OH) are clearly presented. [23] Additionally, the weak peak centered at $\delta$ = -99 ppm shows the existence of Si(2Si, 2Al) or Si(2Si, 1Al, 1OH) sites due to the low Si/Al ratio. [24] In terms of $^{27}$Al NMR, both Meso-Beta and Con-Beta exhibit a pronounced peak centered at around $\delta$ = 55 ppm and a weak peak centered at around $\delta$ = 0 ppm, which are attributed to framework tetrahedral and octahedral aluminium species, respectively. Assuming that the concentration of the tetrahedral and octahedral aluminium are proportional to the respective intensities of the resonances at $\delta$ = 55 ppm and $\delta$ = 0 ppm, the $Al_{Td}/Al_{Oh}$ ratio can be quantified to be 4.42 and 4.10 for Con-Beta and Meso-Beta, respectively. [25] It is well known that calcination in air would induce a partial dealumination process from octahedral aluminum species to tetrahedral aluminum species. [26] Thus the lower $Al_{Td}/Al_{Oh}$ ratio in Meso-Beta implies its more extensive dealumination process due to the more locally developed heat (more entrapped organics) and lower thermal stability (nanocrystallinity) [27].

Thermogravimetric analyses (TGA) were performed to investigate whether cationic polymer N-(2-hydroxy)-propyl-trimethyl ammonium chitosan chloride (HTCC) participated in the synthesis of Meso-Beta. Fig. S2 shows thermogravimetric analysis curves of as-synthesized Con-Beta, as-synthesized Meso-Beta and HTCC. As-synthesized Con-Beta shows a weight loss of 20.9% due to the loss of water and TEA template. While, as-synthesized Meso-Beta displays a weight loss of 21.3%, slightly higher than that of Con-Beta. For both samples, the weight losses below 170 °C can be ascribed to the removal of adsorbed water. Remarkably, a specific weight loss in the region of 170-330 °C is observed for as-synthesized Meso-Beta, which can be ascribed to the initial decomposition of HTCC (Fig. S2b). [28] These results indicate that HTCC patrticipated in the synthesis of Meso-Beta as the meso-template via flocculating effect, giving birth to the intercrystalline mesoporosity. [22a, 29]

Fig. 4 illustrates the temperature-programmed desorption of ammonia (NH$_3$-TPD) profiles on H-type Con-Beta and Meso-Beta with a similar Si/Al ratio. For H-type Con-Beta, the TPD curve shows a gradual rise in the low temperature region, a maximum at 205 °C, and thereafter a decline with a smaller peak appearing at 380 °C. The existence of two TPD peaks means that the H-type Con-Beta has weak as well as strong acid sites. Apparently, H-type Meso-Beta shows a similar TPD profile with lower desorption temperatures (180 °C and 330 °C, respectively) and lower amount of desorbed ammonia, indicating the lower concentration/strength of acid sites in Meso-Beta. Such acidic properties can be probably ascribed to the lower aluminium content, lower crystallinity and lower framework aluminium species in sample Meso-Beta [27, 30].
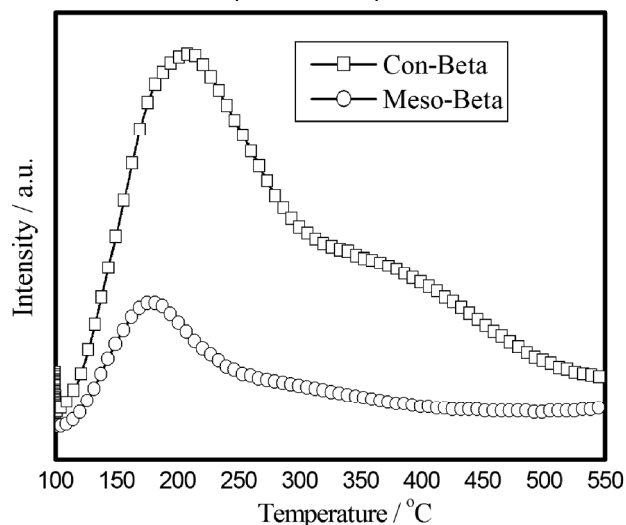


Figure 4. NH$_3$-TPD profiles of H-type Con-Beta and Meso-Beta.

The catalytic performances of H-type Meso-Beta and H-type Con-Beta were tested on the isomerizationm of α-pinene, which is the main ingredient of turpentine. To make the best of this wide-spread bicyclic monoterpene, the value added products of α-pinene isomerization have been widely used in the pharmaceutical and perfume industries. [31] The acid catalysed α-pinene isomerization is a typical weak acid-catalyzed reaction, which can occur on both weak and strong acid sites, [31a] as illustrated in Scheme 1. Table 2 represents the conversion of α-pinene and selectivity to some main products (camphene, limonene, terpinolene, α- and γ-terpinene) over H-type Con-Beta and H-type Meso-Beta, respectively. It is observed that Con-Beta shows a conversion of 21.3%, probably due to the hindrance effect of its intrinsic microporosity. [32] In contrast, Meso-Beta gives an enhanced conversion of 32.2% under the

same conditions, without significant changes in selectivity towards the main products. Considering the higher concentration/strength of acid sites in H-Type Con-Beta, the enhanced catalytic activity may be mainly attributed to the favoured mass transfer in Meso-Beta for both reactants and products, due to the presence of mesopore network.
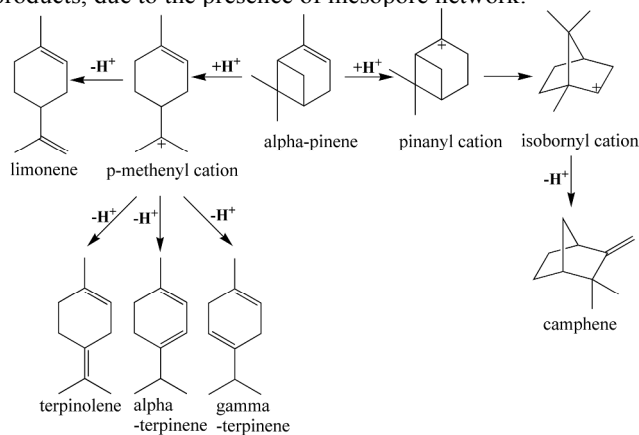


Scheme 1. Reaction pathway for acid-catalyzed α-pinene isomerization.

Table 2. The catalytic performance of the samples. [a]

| Sample | Conversion (%) | Selectivity (%) | | | | | |
|---|---|---|---|---|---|---|---|
| | | Camphene | α-Terpinene | Limonene | γ-Terpinene | Terpinolene | Others |
| Con-Beta | 21.3 | 18.6 | 7.6 | 29.3 | 4.7 | 9.4 | 30.4 |
| Meso-Beta | 32.2 | 19.7 | 7.2 | 30.7 | 4.4 | 8.7 | 29.2 |

[a] Reaction conditions: 70 °C, 30 min, 0.1 g of catalyst, 2.0 mL of α-pinene.

## 2. Mesoporous Sn-Beta

Fig. 5 shows the XRD patterns of H-Al-Meso-Beta, De-Al-Meso-Beta, Meso-Sn-Beta and Con-Sn-Beta. It can be seen that all the samples display the characteristic diffraction peaks associated with BEA topology. The highest diffraction intensity on Con-Sn-Beta suggests its high crystallinity, probably due to the addition of fluoride anion as a mineralizing agent. Meanwhile, the comparable diffraction intensities and microporosity (shown in Table 1) among H-Al-Meso-Beta, De-Al-Meso-Beta and Meso-Sn-Beta indicate the absence of crystalline structure damage during the dealumination and SnCl$_4$ vapor treatment.
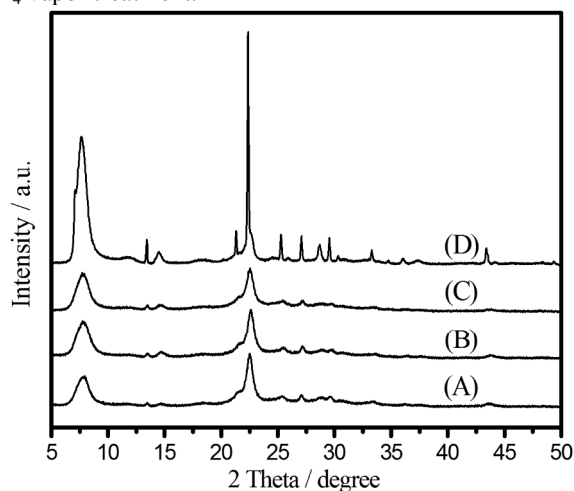


Figure 5. XRD patters of H-Al-Meso-Beta (A), De-Al-Meso-Beta (B), Meso-Sn-Beta (C) and Con-Sn-Beta (D).

UV-Vis spectroscopic technique provides a conventional tool to detect the coordination state of Sn species in Sn-containing metallosilicates. UV-Vis spectra of Meso-Sn-Beta and Con-Sn-Beta are given in Fig. 6. One main absorption band in the region of 210-220 nm relevant to isolated Sn atoms is observed for both Meso-Sn-Beta and Con-Sn-Beta, indicating the presence of isolated, tetrahedrally coordinated Sn$^{IV}$ species within their zeolite frameworks [18e]. These results confirm the applicability of gas-solid reaction to introduce tetrahedrally coordinated Sn species. [18c]
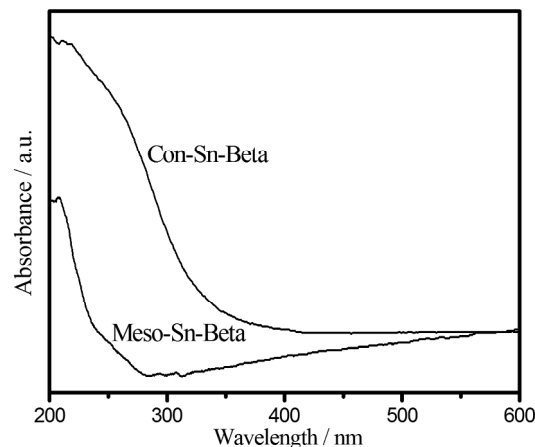


Figure 6. UV-Vis spectra of Meso-Sn-Beta and Con-Sn-Beta.

The N$_2$ adsorption-desorption isotherms and the corresponding pore-size distributions of Meso-Sn-Beta and Con-Sn-Beta are presented in Fig. 7. A high uptake caused by micropore filling is observed at the low relatively pressure (<0.01) for both samples. Unlike the representative Type I (Langmuir) isotherm for Con-Sn-Beta, Meso-Sn-Beta exhibits a mixture of type I and IV, with a larger adsorption amount and a hysteresis loop above the relative pressure of 0.8, suggesting the presence of mesoporosity. According to the BJH pore-size distribution derived from the desorption branch of Meso-Sn-Beta, the mesopore size is estimated to be about 20 ~ 50 nm, in accordance with that of Meso-Beta indicated above. From the structural parameters of the samples listed in Table 1, after a dealumination process and a subsequent solid-gas reaction, Meso-Sn-Beta maintained similar structural features with the parent H-Al-Meso-Beta. It is noteworthy that Meso-Sn-Beta shows higher external specific surface area (218 m$^2$g$^{-1}$), total pore volume (0.51 cm$^3$g$^{-1}$) and external volume (0.34 cm$^3$g$^{-1}$) than those of Con-Beta, due to the preserved hierarchy.
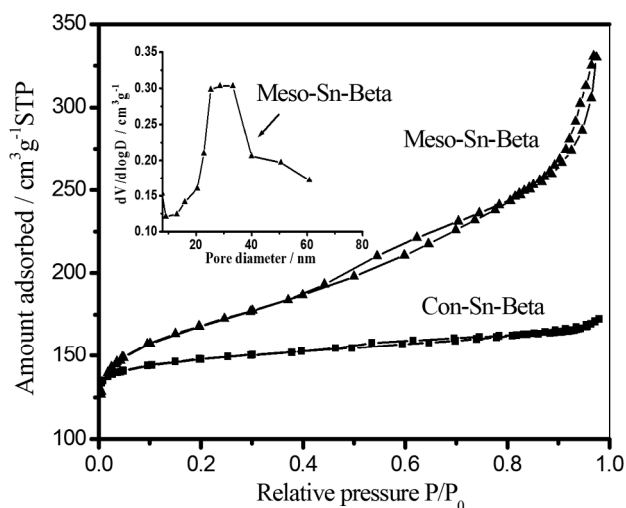
Figure 7. $N_2$ adsorption-desorption isotherms and pore-size distribution curve (inset) of Con-Sn-Beta and Meso-Sn-Beta.

SEM and TEM images of Con-Sn-Beta and Meso-Sn-Beta are given in Fig. 8. Notably, unlike the bulky particles of Con-Sn-Beta (~1 μm, Fig. 8a), Meso-Sn-Beta particles possess similar morphology and structure with the parent material Meso-Beta. Especially, the meso-/microporous structure was well preserved after the dealumination process and the $SnCl_4$ vapor treatment. Thus, Meso-Sn-Beta is expected to suffer from less diffusion limitation to bulky substrate molecules.
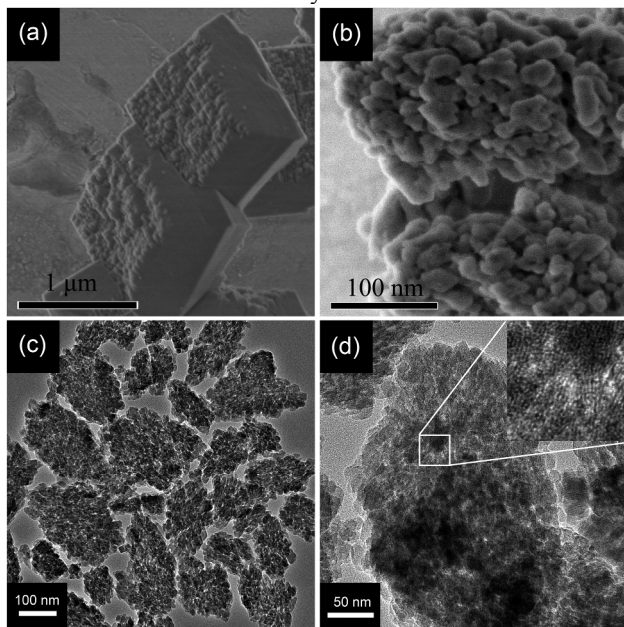


Figure 8. SEM images of Con-Sn-Beta (a) and Meso-Sn-Beta (b); TEM images (c, d) of Meso-Sn-Beta at different magnifications.

To evaluate the catalytic performance of Meso-Sn-Beta for reactions involving bulky molecules, the selective oxidation of 2-adamantanone by $H_2O_2$ in the solvent of chlorobenzene and the isomerization of glucose in water were carried out, as illustrated in Scheme 2. The catalytic data of the samples is summarized in Table 3. In the Baeyer-Villiger oxidation of 2-adamantanone, Meso-Sn-Beta gives a higher conversion (69.1%) than that of Con-Sn-Beta (64.7%) at the similar Sn content. Meanwhile, in the isomerization of glucose, a higher fructose yield (40%) is also observed for Meso-Sn-Beta than that of Con-Sn-Beta (35%). It has been reported that the

hydrophobicity of zeolite catalyst is favorable in both catalytic reactions above. [18c, 33] Taking into account of the more hydrophobic nature on micrometer sized Con-Sn-Beta and the bulky molecular size of the ketone and glucose, the catalytic results observed here suggest the more dominant role of diffusions of reactants and/or products.

Table 3. Catalytic properties of different catalysts.

| Reactions | Con-Sn-Beta | Meso-Sn-Beta |
|---|---|---|
| 2-adamantanone + hydrogen peroxide | 64.7[a] | 69.1 |
| isomerization of glucose | 53.1(35.1)[b] | 82(40) |

[a] The data represents the reactant conversion [%]. The lactone selectivity is higher than 99%.[b] The first data represents the glucose conversion [%]. The number in parenthesis indicates the yield of fructose.
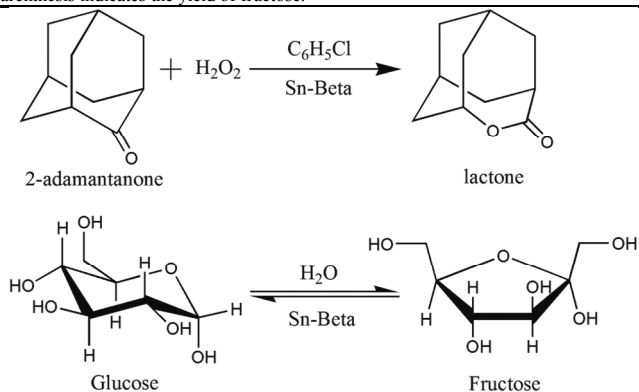


Scheme 2. Baeyer-Villiger oxidation of 2-adamantanone by hydrogen peroxide (top); isomerization of glucose to fructose (bottom).

## Conclusions

In this work, mesostructured Beta and Sn-Beta zeolites have been successfully prepared through a hydrothermal synthesis route in the presence of cationic ammonium-modified chitosan, with the later further by a post-synthetic solid-gas reaction of highly dealuminated mesoporous Beta zeolite with $SnCl_4$ vapor. It is revealed that the addition of cationic chitosan induced the nanocrystal aggregation to particle sizes of ~300 nm, giving rise to the intercrystalline/interparticle mesoporosity. In the Sn-implanting procedure, Sn species are demonstrated to be doped into the framework of the resulting mesoporous Beta zeolite in a tetrahedral environment without structural collapse. Due to the generated meso-/microporous structure, mesoporous Beta and Sn-Beta exhibited significantly higher performances in α-pinene isomerization, selective oxidation of 2-adamantanone by hydrogen peroxide and the isomerization of glucose in water than their counterparts without mesostructure. It is expected that this cascade preparation strategy can be applied to other structured and heteroatom-substituted zeolitic materials.

## Experimental

### 1. Chemicals and synthetic procedures

#### Chemicals

Chitosan (MW ~ 100,000, degree of deacetylation was 95%) was purchased from Zhejiang Golden-Shell pharmaceutical Co., Ltd.. Glycidyltrimethylammonium chloride (GTMAC, 90%), tin chloride (99%), α-pinene (98%) and 2-adamantanone (99%) were obtained from Sigma-Aldrich. Tetraethylammonium

hydroxide (TEAOH, 35%) was purchased from Tokyo Chemical Industry Co., Ltd.. Fumed silica (Aerosil 200) was obtained from Degussa Co., Ltd.. All the rest reagents, including NaOH, NaAlO$_2$, NH$_4$NO$_3$, HNO$_3$, AgNO$_3$, tin (IV) chloride pentahydrate (SnCl$_4$·5H$_2$O), chlorobenzene, glucose and tetraethyl orthosolicate (TEOS) were purchased from Sinopharm Chemical Reagent Co., Ltd. and were reagent grade.

**Preparation of ammonium-modified chitosan**

The ammonium-modified chitosan, N-(2-hydroxy)-propyl-trimethyl ammonium chitosan chloride (HTCC) was prepared by a modified method proposed elsewhere. [20e, 28]

**Synthesis of mesoporous Beta zeolite**

0.12 g NaOH and 0.56 g NaAlO$_2$ were mixed with 11.25 g tetraethylammonium hydroxide (35%, TCI) and stirred for 1 h. Then, 3.6 g fumed silica (Aerosil 200, Degussa) was added into this solution, forming a thick sol after continuous stirring for about 3 h at room temperature. Afterwards, an aqueous solution containing 1.5 g HTCC and 10 g H$_2$O was added dropwise into the resulting mixture under stirring. After stirring overnight, the earth yellow mixture was charged into Teflon-lined steel autoclaves for hydrothermal treatment at 140 °C for 5 days. The product was collected by centrifugation, washed with deionized water until the pH was below 9, dried overnight at 100 °C and calcined at 600 °C for 10 h. The sample is labeled as Meso-Beta. For comparison, conventional Beta zeolite with similar Si/Al ratio was synthesized under the similar procedures in the absence of HTCC solution and labeled as Con-Beta.

For catalysis, H-form Con-Beta and Meso-Beta were obtained by ion exchanges with 1 M NH$_4$NO$_3$ solution at 70 °C for three times and the subsequent calcination in air at 550 °C for 5 h.

**Synthesis of mesoporous Sn-Beta**

Mesoporous Beta zeolite (H-type) obtained above was used as the parent material. Dealumination of H-type mesoporous Beta zeolite (H-Al-Meso-Beta) was performed by treating the parent material with a concentrated nitric acid solution (13 M, 20 mLg$^{-1}$) at 100 °C for 20 h. In the subsequent post-incorporation of Sn species, 0.5 g of dealuminated mesoprous Beta zeolite (De-Al-Meso-Beta, Si/Al>1500) was first pretreated in a quartz tubular reactor at 500 °C for 2 h under a flow of dry N$_2$. Then, the N$_2$ flow was diverted through an anhydrous SnCl$_4$ (99%, Sigma) liquid in a glass bubbler with a flow rate of 0.05 Lmin-1. The flow containing SnCl$_4$ vapor was allowed to contact the zeolite powder for about 10 min. Afterwards, the sample was purged with pure N$_2$ at 500 °C for about 4 h to remove any residual SnCl$_4$ from the zeolite powder. After cooling to the room temperature in N$_2$ atmosphere, the resulting zeolite powder was washed with deionized water extensively until chloride ions were not detected in the filtrate by AgNO3 solution (0.1 M) and then was dried in air at 100 °C overnight. The obtained product was labeled as Meso-Sn-Beta.

For comparison, conventional bulky Sn-Beta with similar Sn content was synthesized directly according to the literature.[19c] The procedures involved dealuminated BEA seeds fabrication and Sn-Beta synthesis. The Sn-Beta crystallization was carried out in a Teflon-lined stainless steel autoclave under static condition at 140 °C for 22 days. And the obtained product was signed as Con-Sn-Beta.

## 2. Characterization

Powder XRD patterns were collected on Bruker D8 Focus diffractometer with a graphite-monochromatized Cu Kα radiation (λ=0.15405 nm), typically run at a voltage of 40 kV and current of 40 mA. The contents of Al and Sn in different samples were determined by the results of inductively coupled plasma analysis (Varian 710-ES). The N$_2$ adsorption isotherms were measured at 77 K using Quantachrome NOVA 4200e after outgassing at 200 °C for 10 h. The specific surface area and pore size distribution were calculated by using the Brunauer-Emmett-Teller (BET) and Barrett-Joyner-Halenda (BJH) method, respectively. The micropore surface area and volume were calculated by the t-plot method, and the total pore volume was evaluated at P/P$_0$=0.98. Field emission scanning electron microscopy (FE-SEM) images were obtained using a FEI Magellan 400 scanning electron microscope. Transmission electron microscopy (TEM) observations were performed on a JEOL-2010F electron microscopy operated at 200 kV. $^{29}$Si and $^{27}$Al MAS NMR spectra were recorded on a Bruker AVANCE 600 spectrometer. The TG analysis was carried out under the air atmosphere at a heating rate of 10 °Cmin$^{-1}$ using a NETZSCH STA 409 PG/PC instrument. Temperature-programmed desorption of ammonia (NH$_3$-TPD) was conducted on a homemade apparatus loaded with 150 mg of sample. The catalyst was pretreated at 550 °C for 1 h and then cooled down to 100 °C under He flow. Pure NH$_3$ was introduced until adsorption saturation was reached. The gaseous or physisorbed NH$_3$ was removed by purging He flow at 100 °C for 1 h. Then the temperature was raised from 100 to 550 °C with a heating rate of 1 °Cmin$^{-1}$ and the desorbed NH$_3$ was detected by gas chromatography. UV-vis spectra were recorded on the Shimadzu UV-310PC spectrometer with BaSO$_4$ as a reference.

## 3. Catalytic reactions

The isomerization was carried out at atmospheric pressure in a glass reactor equipped with a reflux condenser under magnetic stirring. In a typical run, 0.10 g catalyst and 2.0 mL of α-pinene (98%, Sigma) were charged into a glass flask to react at 70 °C for 30 min under magnetic stirring. After fast cooling down to room temperature, the solid catalyst was filtered and the remaining liquid was analyzed by an Agilent 7890 gas chromatograph equipped with a HP-5MS capillary column and interfaced to a 5975C mass-selective detector. Chemstation software was used to collect and analyze the data. The content of each product was calculated using the area normalization method. The Baeyer-Villiger oxidation of 2-adamantanone (99%, Sigma) by hydrogen peroxide was carried out in a 25 mL round-bottomed flask equipped with a reflux condenser. The vessel was charged with 2 mmol of 2-adamantanone, 4 mmol of H$_2$O$_2$ (30 wt%), 50 mg of catalyst and 10 mL of chlorobenzene. The mixture was stirred vigorously at 90 °C for 4 h. After the reaction, the mixture was cooled, centrifuged, and the upper solution was collected by a micro-syringe. The samples were analyzed by GC-MS (Agilent, 7890/5975C). Isomerization experiments were carried out in a stainless steel autoclave (10 mL) heated in a temperature-controlled oil bath. In a typical experiment, 4.1 g of an aqueous solution composed of 10% (wt/wt) glucose and the corresponding catalyst amount to achieve a 1:50 metal:glucose molar ratio were added into the sealed reactor equipped with a magnetic stirring bar. The reactor was placed in a 110 °C oil bath and removed after 30 min. The reaction was stopped by cooling the reactor in an ice bath and the samples were analyzed by means of high performance liquid chromatography (HPLC) using an Agilent 1200 system.

## Acknowledgements

## Notes and references

*a* School of Materials Science and Engineering, East China University of Science and Technology, No. 130 Mei-long Road, Shanghai 200237 (P.R. China), Fax: (+86) 21-64250740, E-mail: ysli@ecust.edu.cn

*b* Shanghai Key Laboratory of Functional Materials Chemistry, East China University of Science and Technology, No. 130 Mei-long Road, Shanghai 200237 (P.R. China)

*c* State Key Laboratory of High Performance Ceramics and Superfine Microstructures, Shanghai Institute of Ceramics, Chinese Academy of Science, No. 1295 Ding-xi Road, Shanghai 200050 (P.R. China), E-mail: jlshi@mail.sic.ac.cn

† Footnotes should appear here. These might include comments relevant to but not central to the matter under discussion, limited experimental and spectral data, and crystallographic data.

Electronic Supplementary Information (ESI) available: [details of any supplementary information available should be included here]. See DOI: 10.1039/b000000x/

1   (a) A. Corma, *Chem. Rev.,* 1997, **97**, 2373-2420; (b) M. E. Davis, *Nature*, 2002, **417**, 813-821; (c) A. Corma and H. García, *Chem. Rev.*, 2002, **102**, 3837-3892; (d) I. W. C. E. Arends, R. A. Sheldon, M. Wallau and U. Schuchardt, *Angew. Chem. Int. Ed.*, 1997, **36**, 1144-1163; (e) J. Shi, *Chem. Rev.*, 2012, **113**, 2139-2181; (f) M. Moliner, *Dalton Trans.*, 2014, **43**, 4197-4208.

2   (a) B. J. Schoeman, J. Sterte and J. E. Otterstedt, *Zeolites*, 1994, **14**, 110-116; (b) M. Hartmann, *Angew. Chem. Int. Ed.*, 2004, **43**, 5880-5882.

3   (a) N. S. Nesterenko, F. Thibault-Starzyk, V. Montouillout, V. V. Yuschenko, C. Fernandez, J. P. Gilson, F. Fajula and I. I. Ivanova, *Microporous Mesoporous Mater.*, 2004, **71**, 157-166; (b) Y. Tao, H. Kanoh, L. Abrams and K. Kaneko, *Chem. Rev.*, 2006, **106**, 896-910; (c) J. Perez-Ramirez, C. H. Christensen, K. Egeblad, C. H. Christensen and J. C. Groen, *Chem. Soc. Rev.*, 2008, **37**, 2530-2542; (d) P. Wu, T. Tatsumi, T. Komatsu and T. Yashima, *J. Catal.*, 2001, **202**, 245-255.

4   (a) C. Madsen and C. J. H. Jacobsen, *Chem. Commun.*, 1999, **8**, 673-674; (b) R. Srivastava, N. Iwasa, S.-i. Fujita and M. Arai, *Chem. Eur. J.*, 2008, **14**, 9507-9511.

5   J. Jiang, J. L. Jorda, J. Yu, L. A. Baumes, E. Mugnaioli, M. J. Diaz-Cabanas, U. Kolb and A. Corma, *Science*, 2011, **333**, 1131-1134.

6   (a) F. Ocampo, H. S. Yun, M. M. Pereira, J. P. Tessonnier and B. Louis, *Cryst. Growth Des.*, 2009, **9**, 3721-3729; (b) A. Sachse, A. Galarneau, F. Di Renzo, F. Fajula and B. Coq, *Chem. Mater.*, 2010, **22**, 4123-4125.

7   (a) V. Sebastian, I. Diaz, C. Tellez, J. Coronas and J. Santamaria, *Adv. Funct. Mater.*, 2008, **18**, 1314-1320; (b) H. Mori, K. Aotani, N. Sano and H. Tamon, *J. Mater. Chem.*, 2011, **21**, 5677-5681; (c) L.-H. Chen, X.-Y. Li, J. C. Rooke, Y.-H. Zhang, X.-Y. Yang, Y. Tang, F.-S. Xiao and B.-L. Su, *J. Mater. Chem.*, 2012, **22**, 17381-17403; (d) D. P. Serrano, J. M. Escola and P. Pizarro, *Chem. Soc. Rev.*, 2013, **42**, 4004-4035; (e) K. Moller and T. Bein, *Chem. Soc. Rev.*, 2013, **42**, 3689-3707.

8   (a) M. A. Camblor, A. Corma and S. Valencia, *Microporous Mesoporous Mater.*, 1998, **25**, 59-74; (b) J.-M. Nhut, L. Pesant, J.-P. Tessonnier, G. Winé, J. Guille, C. Pham-Huu and M.-J. Ledoux, *Appl. Catal. A*, 2003, **254**, 345-363; (c) K. Möller, B. Yilmaz, U. Müller and T. Bein, *Chem. Eur. J.*, 2012, **18**, 7671-7674.

9   (a) A. Corma, M. J. Diaz-Cabanas, F. Rey, S. Nicolopoulus and K. Boulahya, *Chem. Commun.*, 2004, **12**, 1356-1357; (b) J. Sun, C. Bonneau, A. Cantin, A. Corma, M. J. Diaz-Cabanas, M. Moliner, D. Zhang, M. Li and X. Zou, *Nature*, 2009, **458**, 1154-1157; (c) T. Willhammar, J. Sun, W. Wan, P. Oleynikov, D. Zhang, X. Zou, M. Moliner, J. Gonzalez, C. Martínez, F. Rey and A. Corma, *Nature Chem.*, 2012, **4**, 188-194.

10   R. Chal, C. Gérardin, M. Bulut and S. van Donk, *ChemCatChem*, 2011, **3**, 67-81.

11   M. S. Holm, E. Taarning, K. Egeblad and C. H. Christensen, *Catal. Today*, 2011, **168**, 3-16.

12   (a) C. J. H. Jacobsen, C. Madsen, I. Houzvicka, I. Schmidt and A. Carlsson, *J. Am. Chem. Soc.*, 2000, **122**, 7116-7117; (b) M. Kustova, P. Hasselriis and C. Christensen, *Catal. Lett.*, 2004, **96**, 205-211; (c) F.-S. Xiao, L. Wang, C. Yin, K. Lin, Y. Di, J. Li, R. Xu, D. S. Su, R. Schlögl, T. Yokoi and T. Tatsumi, *Angew. Chem. Int. Ed.*, 2006, **45**, 3090-3093; (d) H. Wang and T. J. Pinnavaia, *Angew. Chem. Int. Ed.*, 2006, **45**, 7603-7606; (e) M. Choi, H. S. Cho, R. Srivastava, C. Venkatesan, D.-H. Choi and R. Ryoo, *Nat. Mater.*, 2006, **5**, 718-723; (f) D. P. Serrano, J. Aguado, J. M. Escola, J. M. Rodríguez and Á. Peral, *Chem. Mater.*, 2006, **18**, 2462-2464; (g) J. Zhou, Z. Hua, W. Wu, Z. Liu, Y. Zhu, Y. Chen and J. Shi, *Dalton Trans.*, 2011, **40**, 12667-12669.

13   (a) M. Choi, K. Na, J. Kim, Y. Sakamoto, O. Terasaki and R. Ryoo, *Nature*, 2009, **461**, 246-249; (b) K. Na, C. Jo, J. Kim, K. Cho, J. Jung, Y. Seo, R. J. Messinger, B. F. Chmelka and R. Ryoo, *Science*, 2011, **333**, 328-332; (c) L. Wu, V. Degirmenci, P. C. M. M. Magusin, B. M. Szyja and E. J. M. Hensen, *Chem. Commun.*, 2012, **76**, 9492-9494; (d) X. Zhang, D. Liu, D. Xu, S. Asahina, K. A. Cychosz, K. V. Agrawal, Y. Al Wahedi, A. Bhan, S. Al Hashimi, O. Terasaki, M. Thommes and M. Tsapatsis, *Science*, 2012, **336**, 1684-1687; (e) J. Zhu, Y. Zhu, L. Zhu, M. Rigutto, A. V. D. Made, C. Yang, S. Pan, L. Wang, L. Zhu, Y. Jin, Q. Sun, Q. Wu, X. Meng, D. Zhang, Y. Han, J. Li, Y. Chu, A. Zheng, S. Qiu, X. Zheng and F. S. Xiao, *J. Am. Chem. Soc.*, 2014, **136**, 2503-2510.

14   (a) M. D. González, Y. Cesteros and P. Salagre, *Microporous and Mesoporous Mater.*, 2011, **144**, 162-170; (b) P. Kortunov, S. Vasenkov, J. Kärger, R. Valiullin, P. Gottschalk, M. Fé Elía, M. Perez, M. Stöcker, B. Drescher, G. McElhiney, C. Berger, R. Gläser and J. Weitkamp, *J. Ame. Chem. Soc.*, 2005, **127**, 13055-13059; (c) M. Ogura, S.-y. Shinomiya, J. Tateno, Y. Nara, E. Kikuchi and M. Matsukata, *Chem. Lett.*, 2000, **29**, 882-883; (d) D. Verboekend and J. Perez-Ramirez, *Catal. Sci. Technol.*, 2011, **1**, 879-890.

15   (a) K. Na, M. Choi and R. Ryoo, *J. Mater. Chem.*, 2009, **19**, 6713-6719; (b) R. Kore, B. Satpati and R. Srivastava, *Chem. Eur. J.*, 2011, **17**, 14360-14365; (c) K. Möller, B. Yilmaz, R. M. Jacubinas, U. Müller and T. Bein, *J. Am. Chem. Soc.*, 2011, **133**, 5284-5295; (d) L.-H. Chen , X.-Y. Li, G. Tian, Y. Li, J. C. Rooke, G.-S. Zhu, S.-L. Qiu, X.-Y. Yang and B.-L. Su, *Angew. Chem. Int. Ed.*, 2011, **50**, 11156-11161; (e) K. Möller, B. Yilmaz, U. Müller and T. Bein, *Chem. Eur. J.*, 2012, **18**, 7671-7674.

16   X. Meng, F. Nawaz and F.-S. Xiao, *Nano Today*, 2009, **4**, 292-301.

17   (a) H. Kessler, J. Patarin and C. Schott-Darie, *Stud. Surf. Sci. Catal.*, 1994, **85**, 75-113; (b) P. S. Niphadkar, A. C. Garade, R. K. Jha, C. V. Rode and P. N. Joshi, *Microporous Mesoporous Mater.*, 2010, **136**, 115-125; (c) A. Corma, L. T. Nemeth, M. Renz and S. Valencia, *Nature*, 2001, **412**, 423-425; (d) M. Moliner, Y. Román-Leshkov and M. E. Davis, *Proc. Natl. Acad. Sci. USA*, 2010, **107**, 6164-6168.

18   (a) B. Kraushaar and J. H. C. Hooff, *Catal. Lett.*, 1988, **1**, 81-84; (b) J. Gao, J. Liu, X. Wang and X. Guo, *Ind. Eng. Chem. Res.*, 2010, **49**, 2194-2199; (c) P. Li, G. Liu, H. Wu, Y. Liu, J.-g. Jiang and P. Wu, *J. Phys. Chem. C*, 2011, **115**, 3663-3670; (d) C. Hammond, S. Conrad and I. Hermans, *Angew. Chem. Int. Ed.*, 2012, **51**, 11736-11739; (e) P. Wolf, C. Hammond, S. Conrad and I. Hermans, *Dalton Trans.*, 2014, **43**, 4514-4519.

19   (a) M. S. Holm, S. Saravanamurugan and E. Taarning, *Science*, 2010, **328**, 602-605; (b) V. Choudhary, A. B. Pinar, S. I. Sandler, D. G. Vlachos and R. F. Lobo, *ACS Catal.*, 2011, **1**, 1724-1728; (c) C. M. Lew, N. Rajabbeigi and M. Tsapatsis, *Microporous Mesoporous Mater.*, 2012, **153**, 55-58.

20   (a) H. Wu, B. Zheng, X. Zheng, J. Wang, W. Yuan and Z. Jiang. *J. Power Sources*, 2007, **173**, 842-852; (b) Y. Wang, D. Yang, X. Zheng, Z. Jiang and J. Li, *J. Power Sources*, 2008, **183**, 454-463; (c) Y. Wang, Z. Jiang, H. Li and D. Yang, *Chem. Eng. Process*, 2010, **49**, 278-285; (d) J. Ma and Y. Sahai, *Carbohydr. Polym.* , 2013, **92**, 955-975; (e) J. Jin, X. Zhang, Y. Li, H. Li, W. Wu, Y. Cui, Q. Chen, L. Li, J. Gu, W. Zhao and J. Shi, *Chem. Eur. J.*, 2012, **18**, 16549-16555; (f) J. Yao, Y. Huang and H. Huang, *J. Mater. Chem.*, 2010, **20**, 9827-9831.

21   M. M. J. Treacy and J. B. Higgins, Collection of simulated XRD powder patters for zeolites, Elsevier, 2001.

**Dalton Transactions Accepted Manuscript**

22   (a) J. Song, L. Ren, C. Yin, Y. Ji, Z. Wu, J. Li, and F.-S. Xiao, *J. Phys. Chem. C*, 2008, **112**, 8609-8613; (b) H. Zhu, Z. Liu, D. Kong, Y. Wang and Z. Xie, *J. Phys. Chem. C*, 2008, **112**, 17257-17264; (c) C. Yin, D. Tian, M. Xu, Y. Wei, X. Bao, Y. Chen and F. Wang, *J. Colloid Interface Sci.*, 2013, **397**, 108-113.

23   S. Mintova, V. Valtchev, T. Onfroy, C. Marichal, H. Knözinger and T. Bein, *Microporous Mesoporous Mater.*, 2006, **90**, 237-245.

24   (a) M. A. Camblor, A. Corma and S. Valencia, *Micporous Meoporous Mater.*, 1998, **25**, 59-74; (b) J. Pérez-Pariente, J. Sanz, V. Fornés and A. Corma, *J. Catal.*, 1990, **124**, 217-223; (c) Z. Xie, J. Bao, Y. Yang, Q. Chen and C. Zhang, *J. Catal.*, 2002, **205**, 58-66.

25   (a) B. Chakraborty and B. Viswanathan, *Catal. Today*, 1999, **49**, 253-260; (b) R. Hajjar, Y. Millot, P. P. Man, M. Che and S. Dzwigaj, *J. Phys. Chem. C*, 2008, **122**, 20167-20175.

26   (a) I. Kiricsi, C. Flego, G. Pazzuconi, W. O. Parker, Jr., R. Millini, C. Perego and G. Bellussi, *J. Phys. Chem.*, 1994, **98**, 4627-4634; (b) A. Omegna, J. A. van Bokhoven and R. Prins, *J. Phys. Chem. B*, 2003, **107**, 8854-8860.

27   M. A. Camblor, A. Corma and S. Valencia, *Microporous Mesoporous Mater.*, 1998, **25**, 59-74.

28   C.-W. Nam, Y.-H. Kim and S.-W. Ko, *J. Appl. Polym. Sci.*, 1999, **74**, 2258-2265.

29   K. Möller, B. Yilmaz, U. Müller and T. Bein, *Chem. Mater.*, 2011, **23**, 4301-4310.

30   (a) J. Zhou, Z. Liu, L Li, Y. Wang, H. Gao, W. Yang, Z. Xie and Y. Tang, *Chin. J. Catal.*, 2013, **34**, 1429-1433; (b) A. Corma, *J. Catal.*, 2003, **216**, 298-312.

31   (a) A. Corma, S. Iborra and A. Velty, *Chem. Rev.*, 2007, **107**, 2411-2502; (b) K. A. d. S. Rocha, P. A. Robles-Dutenhefner, I. V. Kozhevnikov and E. V. Gusevskaya, *Appl. Catal. A*, 2009, **352**, 188-192.

32   (a) Y. Wu, F. Tian, J. Liu, D. Song, C. Jia and Y. Chen, *Microporous Mesoporous Mater.*, 2012, **162**, 168-174; (b) G. Gündüz, R. Dimitrova, S. Yilmaz, L. Dimitrov and M. Spassova, *J. Mol. Catal. A: Chem.*, 2005, **225**, 253-258.

33   R. Bermejo-Deval, R. Gounder and M. E. Davis, *ACS Catal.*, 2012, **2**, 2705-2713.

# Synthesis of mesoporous Beta and Sn-Beta zeolites and their catalytic performances

Junjiang Jin, Xinxin Ye, Yongsheng Li, Yanqin Wang, Liang Li, Jinlou Gu, Wenru Zhao and Jianlin Shi

Text: Mesoporous Beta and Sn-Beta zeolites have been successfully synthesized through a hydrothermal templating and a subsequent post-synthetic route, respectively.

Colour graphic: